64 (2019) APPLICATIONS OF MATHEMATICS No. 2, 225–251

ON SUITABLE INLET BOUNDARY CONDITIONS FOR FLUID-STRUCTURE INTERACTION PROBLEMS IN A CHANNEL

Jan Valášek, Petr Sváček, Jaromír Horáček, Praha

Received September 30, 2018. Published online March 18, 2019.

Abstract. We are interested in the numerical solution of a two-dimensional fluid-structure interaction problem. A special attention is paid to the choice of physically relevant inlet boundary conditions for the case of channel closing. Three types of the inlet boundary conditions are considered. Beside the classical Dirichlet and the do-nothing boundary conditions also a generalized boundary condition motivated by the penalization prescription of the Dirichlet boundary condition is applied. The fluid flow is described by the incompressible Navier-Stokes equations in the arbitrary Lagrangian-Eulerian (ALE) form and the elastic body creating a part of the channel wall is modelled with the aid of linear elasticity. Both models are coupled with the boundary conditions prescribed at the common interface.

The elastic and the fluid flow problems are approximated by the finite element method. The detailed derivation of the weak formulation including the boundary conditions is presented. The pseudo-elastic approach for construction of the ALE mapping is used. Results of numerical simulations for three considered inlet boundary conditions are compared. The flutter velocity is determined for a specific model problem and it is shown that the boundary condition with the penalization approach is suitable for the case of the fluid flow in a channel with vibrating walls.

Keywords: flow-induced vibration; 2D incompressible Navier-Stokes equations; linear elasticity; inlet boundary conditions; flutter instability

MSC 2010: 76D05, 65N30, 65N12

1. Introduction

The fluid-structure interaction (FSI) problems need to be taken into account in many technical applications, see e.g. [7]. Classical examples are the bridge or the

Authors acknowledge support from the ESIF, EU Operational Programme Research, Development and Education, and from the Center of Advanced Aerospace Technology (CZ.02.1.01/0.0/0.0/16_019/0000826), Faculty of Mechanical Engineering, Czech Technical University in Prague and by Grant No. GA16-01246S of Czech Science Foundation.

airfoil design, [8]. Another important application is for example the liquid packing system, see [11], or the paper transport in printing machines, see [23]. The aim of this paper is to investigate the problem of FSI simulation in a channel with flexible walls. Such problems can be found besides technical applications also in biomechanical applications, see e.g. [2].

The presented FSI problem is the non-linear problem consisting of two time dependent subproblems, the fluid flow problem and the elastic structure deformation problem, which are coupled by the boundary conditions at the common interface. Further, due to the considered geometry the flow accelerates at the channel constriction. Consequently, the fluid flow behind the channel constriction has usually quite complex structure, but still the peak velocities are usually lower than 0.3 Mach. Therefore, the fluid flow in this channel can be modelled as incompressible. However, the changes of the flow domain in time cannot be neglected, and mesh moving methods based on the arbitrary Lagrangian-Eulerian (ALE) method, the immersed boundary method or the overset method based on projection between the local fine and the global coarse grids are inevitably used, see e.g. [27], [22] or [21], respectively. Due to the coupled nature of the FSI problem the fluid flow and elastic subproblems need to be solved simultaneously with strong coupling procedure in order to obtain more accurate and robust numerical method, see [19]. This results in high computational costs.

The FSI systems are sensitive to setup of many input parameters. Beside the dependence on the fluid and structure material parameters and the geometry of the problem, it can be a less expected dependence on the length of the inflow channel, see [5], [26]. Further, it was shown that the system behaviour also principally depends on the artificially chosen boundary conditions at the inlet and outlet, see e.g. [25], [26].

Let us emphasize that the influence of the inlet boundary conditions for the incompressible flow is even more important during the periodic closure of the channel. The two frequently used possibilities are to prescribe the inlet velocity or the inlet pressure, see [13]. In the finite element (FE) context these boundary conditions are realized by the Dirichlet boundary condition or a suitable modification of the do-nothing boundary condition, see [3]. For the incompressible flow model the use of the Dirichlet boundary condition leads to high, unphysical oscillations of the inlet pressure values during the channel closing phase, see [30]. On the other hand the prescription of the inlet pressure (i.e. pressure gradient between inlet and outlet) results in significant oscillations of the inlet velocity keeping the pressure gradient constant, which was not observed experimentally, see e.g. [14]. A remedy for this situation seems to be newly proposed penalization approach published in [26] for a simplified FSI problem.

This approach is similar to the weakly enforced Dirichlet boundary condition often used in the discontinuous-Galerkin method, see e.g. [9]. It also reminds the realization of the Dirichlet boundary condition for a scalar problem in [1]. It can be seen as a generalization between the velocity and the pressure driven FSI problem. The choice of the parameter $\varepsilon \in (0, \infty)$ switches between the two limit cases of the system behaviour given by the Dirichlet and do-nothing boundary conditions. A similar approach is used in [15], where the switching between the computed pressure and the prescribed nominal pressure is realized during the channel closure in a substantially simplified model.

The aim of the present paper is to extend the solution of the FSI problem studied in [26], where the structure is modelled as an elastically supported solid body with two degrees of freedom (2DOF). Here, the two-dimensional (2D) Navier-Stokes equations are coupled with a structure modelled with the aid of the continuum model. This substantially complicates the numerical solution, but affords better approximation of the structure interface deformation, allowing to determine more precisely the whole numerical solution of FSI (since it depends on the interface position itself) and to capture such phenomena like flow separation point and mucosal waves, which cannot be obtained by the simplified model of the solid body. On the other hand, a more general and robust moving mesh algorithm is needed.

The second important extension of the results obtained in [26] is the parametric study of FSI simulation behaviour with the inlet boundary condition implemented by the penalization approach. The dependence of the inlet pressure and the inlet flow rate on the penalization parameter ε and the minimal half-gap of the channel is studied in the present paper.

For the numerical approximation of both subproblems the finite element method (FEM) is used. The elastic deformation is for simplicity described by the linear elasticity theory. Further, to address all problems associated with the numerical simulations of viscous, incompressible, high Reynolds number flows the FEM with the streamline-upwind/Petrov-Galerkin (SUPG), pressure-stabilization/Petrov-Galerkin (PSPG) and 'div-div' stabilization procedures are applied, see [12], [10]. In order to reduce the computational costs and to simplify the problem the symmetric configuration of the channel is considered. The ALE method is applied, where for the ALE mapping the pseudo-elastic approach instead of other possibilities like linear interpolation or elliptic smoothing is chosen, see e.g. [20]. The main advantages of this approach are robustness, easy implementation and the possibility to easily tune the pseudo-elastic parameters controlling deformations of the FE mesh.

The paper is structured as follows. The mathematical description of FSI problem including all the considered boundary conditions is given in the first section. The second section contains the detailed description of the numerical scheme, particularly

the implementation of the inlet boundary conditions and the stabilization of the fluid flow. In the third section the numerical results are presented and the behaviour of the studied system in dependence of the boundary conditions used are discussed.

2. Mathematical model

The considered configuration of a two-dimensional FSI model problem is shown in Figure 1. It consists of the fluid (Ω^{f}) and the structure (Ω^{s}) domains in the reference and deformed states. The domain $\Omega^{\mathrm{s}}_{\mathrm{ref}}$ denotes the reference state of the elastic structure. The domain $\Omega^{\mathrm{f}}_{\mathrm{ref}}$ represents the reference fluid domain, i.e. the domain at the time instant $t = 0$. The common interface between the fluid and the structure domain is denoted as $\Gamma_{\mathrm{W}_{\mathrm{ref}}} = \Gamma_{\mathrm{W}_0}$.

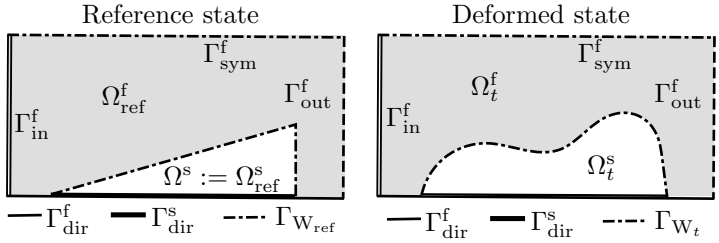

Figure 1. Scheme of FSI configuration in the reference state on the left and after undergoing a deformation at arbitrary time t on the right. The FSI domain is composed of the elastic structure domain Ω^{s} and the fluid domain Ω^{f}_t together with the boundaries: inlet $\Gamma^{\mathrm{f}}_{\mathrm{in}}$, outlet $\Gamma^{\mathrm{f}}_{\mathrm{out}}$, boundary of symmetry $\Gamma^{\mathrm{f}}_{\mathrm{sym}}$, wall $\Gamma^{\mathrm{f}}_{\mathrm{dir}}$ and interface Γ_{W_t}.

For the description of the elastic structure deformation the Lagrange coordinates are used, i.e. the computational domain at arbitrary time t is set to $\Omega^{\mathrm{s}} = \Omega^{\mathrm{s}}_{\mathrm{ref}}$. The change of the fluid reference domain $\Omega^{\mathrm{f}}_{\mathrm{ref}}$ with the reference interface $\Gamma_{\mathrm{W}_{\mathrm{ref}}}$ to the domain Ω^{f}_t and to the interface Γ_{W_t} at any time instant t is determined by the motion of the elastic structure Ω^{s} (and the interface $\Gamma_{\mathrm{W}_{\mathrm{ref}}}$) and treated with the aid of the ALE method.

2.1. Elastic body. The deformation of the elastic body Ω^{s} is described with the aid of a displacement $\mathbf{u}(X,t) = (u_1, u_2)$ of a point $X \in \Omega^{\mathrm{s}}$. The structure motion is then modelled by the partial differential equation

$$\varrho^{\mathrm{s}} \frac{\partial^2 u_i}{\partial t^2} - \frac{\partial \tau^{\mathrm{s}}_{ij}(\mathbf{u})}{\partial X_j} = f^{\mathrm{s}}_i \quad \text{in } \Omega^{\mathrm{s}} \times (0,T), \tag{2.1}$$

where the symbol ϱ^{s} denotes the structure density, the tensor τ^{s}_{ij} is the Cauchy stress tensor, the vector $\mathbf{f}^{\mathrm{s}} = (f^{\mathrm{s}}_1, f^{\mathrm{s}}_2)$ describes the density of the volume force and $X = (X_1, X_2)$ are the reference coordinates.

Assuming that the stress is substantially lower than the yield strength the Cauchy stress tensor can be expressed with help of the generalized Hook law, see e.g. [24]. For the isotropic structure it has the form

$$\tau_{ij}^{\mathrm{s}} = \lambda^{\mathrm{s}}(\operatorname{div}\mathbf{u})\delta_{ij} + 2\mu^{\mathrm{s}} e_{ij}^{\mathrm{s}}, \tag{2.2}$$

where λ^{s}, μ^{s} are Lamé constants depending on the Young modulus of elasticity E^{s} and the Poisson ratio σ^{s}. The tensor δ_{ij} is the Kronecker delta and the tensor $\mathbf{e}^{\mathrm{s}} = (e_{ij}^{\mathrm{s}})$ is the strain tensor, which for the assumption of small displacements simplifies to the form

$$e_{ij}^{\mathrm{s}} = \frac{1}{2}\Big(\frac{\partial u_i}{\partial X_j} + \frac{\partial u_j}{\partial X_i}\Big). \tag{2.3}$$

The elastic problem (2.1) is supplied with the initial and boundary conditions

$$\begin{aligned}
&\text{a)} \quad \mathbf{u}(X,0) = \mathbf{u}_0(X) && \text{for } X \in \ \Omega^{\mathrm{s}},\\
&\text{b)} \quad \frac{\partial \mathbf{u}}{\partial t}(X,0) = \mathbf{u}_1(X) && \text{for } X \in \ \Omega^{\mathrm{s}},\\
&\text{c)} \quad \mathbf{u}(X,t) = \mathbf{u}_{\mathrm{dir}}(X,t) && \text{for } X \in \Gamma_{\mathrm{dir}}^{\mathrm{s}},\ t \in (0,\mathrm{T}),\\
&\text{d)} \quad \tau_{ij}^{\mathrm{s}}(X,t) n_j^{\mathrm{s}}(X) = q_i^{\mathrm{s}}(X,t) && \text{for } X \in \Gamma_{\mathrm{W_{ref}}},\ t \in (0,\mathrm{T}),
\end{aligned} \tag{2.4}$$

where the $\Gamma_{\mathrm{W_{ref}}}, \Gamma_{\mathrm{dir}}^{\mathrm{s}}$ are mutually disjoint parts of the boundary, i.e. $\partial\Omega^{\mathrm{s}} = \Gamma_{\mathrm{W_{ref}}} \cup \Gamma_{\mathrm{dir}}^{\mathrm{s}}$ (see Figure 1) and $n_j^{\mathrm{s}}(X)$ are the components of the unit outer normal to $\partial\Omega^{\mathrm{s}}$. The vector $\mathbf{q}^{\mathrm{s}} = (q_1, q_2)$ represents the aerodynamic forces acting on the interface $\Gamma_{\mathrm{W_{ref}}}$.

2.2. ALE method. The ALE method enables to treat the fluid domain changes. The cornerstone of this method is the assumed existence of a diffeomorphism A_t which maps the reference (undistorted) domain $\Omega_{\mathrm{ref}}^{\mathrm{f}}$ onto the domain Ω_t^{f} at any instant time $t \in (0,T)$, i.e. $x = A_t(X)$. The mapping A_t is desired to fulfil the conditions

$$\frac{\partial A_t}{\partial t} \in C^1(\overline{\Omega_{\mathrm{ref}}^{\mathrm{f}}}), \quad A_t(\partial\Omega_{\mathrm{ref}}^{\mathrm{f}}) = \partial\Omega_t^{\mathrm{f}}, \quad t \in (0,T). \tag{2.5}$$

Particularly it means that the boundary $\partial\Omega_t^{\mathrm{f}} \setminus \Gamma_{\mathrm{W}_t}$ is fixed and $A_t(\Gamma_{\mathrm{W_{ref}}}) = \Gamma_{\mathrm{W}_t}$, where the location of the interface Γ_{W_t} is given by the deformation $\mathbf{u}$ at time instant t. Let us use the following notation: for an arbitrary function $f(x,t)$ defined for $x \in \Omega_t^{\mathrm{f}}$ the function $\hat{f}(X,t)$ is defined for any $X \in \Omega_{\mathrm{ref}}^{\mathrm{f}}$ as $\hat{f}(X,t) = f(A_t(X),t)$.

The ALE domain velocity $\mathbf{w}_D$ is given as

$$\mathbf{w}_D(x,t) = \widehat{\mathbf{w}}_D(X,t) = \frac{\partial}{\partial t} A_t(X), \quad t \in (0,T),\ X \in \Omega^{\mathrm{f}}_{\mathrm{ref}}. \tag{2.6}$$

The time derivative of an arbitrary continuous function $f(x,t) = f(A_t(X),t)$ with respect to a fixed point $X \in \Omega^{\mathrm{f}}_{\mathrm{ref}}$ is defined as the ALE derivative. It can be shown that it satisfies

$$\frac{D^A}{Dt} f(x,t) = \frac{\partial f}{\partial t}(A_t(X),t) = \frac{\partial f}{\partial t}(x,t) + \mathbf{w}_D(x,t) \cdot \nabla f(x,t). \tag{2.7}$$

More details can be found e.g. in [27] or [10].

2.3. Fluid flow. The flow of the viscous incompressible fluid in Ω^{f}_t is modelled by the Navier-Stokes equations in the ALE form

$$\frac{D^A \mathbf{v}}{Dt} + ((\mathbf{v} - \mathbf{w}_D) \cdot \nabla)\mathbf{v} - \nu^{\mathrm{f}} \Delta \mathbf{v} + \nabla p = \mathbf{0}, \quad \operatorname{div} \mathbf{v} = 0 \quad \text{in } \Omega^{\mathrm{f}}_t, \tag{2.8}$$

where $\mathbf{v}(x,t)$ denotes the fluid velocity, $p(x,t)$ is the kinematic pressure (i.e. the pressure divided by the constant density ϱ^{f}) and ν^{f} is the kinematic fluid viscosity, see [10].

Equations (2.8) are completed by the initial condition $\mathbf{v}(x,0) = \mathbf{v}_0(x)$ and the boundary conditions for any $t \in (0,T)$

$$\begin{aligned}
&\text{a) } \mathbf{v}(x,t) = \mathbf{0} && \text{for } x \in \Gamma^{\mathrm{f}}_{\mathrm{dir}},\\
&\text{b) } \mathbf{v}(x,t) = \mathbf{w}_D(x,t) && \text{for } x \in \Gamma_{\mathrm{W}_t},\\
&\text{c) 1) } \mathbf{v}(x,t) \cdot \mathbf{n}^{\mathrm{f}} = 0 && \text{for } x \in \Gamma^{\mathrm{f}}_{\mathrm{sym}},\\
&\quad \text{2) } \frac{\partial(\mathbf{v} \cdot \mathbf{t}^{\mathrm{f}})}{\partial \mathbf{n}^{\mathrm{f}}} = 0,\\
&\text{d) } (p(x,t) - p_{\mathrm{ref}})\mathbf{n}^{\mathrm{f}} = \nu^{\mathrm{f}} \frac{\partial \mathbf{v}}{\partial \mathbf{n}^{\mathrm{f}}} - \frac{1}{2}\mathbf{v}(\mathbf{v} \cdot \mathbf{n}^{\mathrm{f}})^- && \text{for } x \in \Gamma^{\mathrm{f}}_{\mathrm{out}},
\end{aligned} \tag{2.9}$$

where vectors $\mathbf{n}^{\mathrm{f}}$ and $\mathbf{t}^{\mathrm{f}}$ are the unit outer normal and the unit tangent to the boundary $\partial\Omega^{\mathrm{f}}_t$, respectively. Symbol $(\alpha)^-$ denotes the negative part of any real number α defined as $\alpha^- = \min\{0,\alpha\}$ and p_{ref} is the reference pressure. The symmetry boundary condition in the considered case of $\Gamma^{\mathrm{f}}_{\mathrm{sym}} = \{x_1 \in [x_{\min}, x_{\max}],\ x_2 = 0\}$ has the form $v_2(x,t) = 0$, $\partial v_1/\partial x_2 = 0$.

The p_{ref} is set as zero at the outlet $\Gamma^{\mathrm{f}}_{\mathrm{out}}$. The outlet boundary condition (2.9) d) is a modified formulation of the do-nothing boundary condition and suppresses a possible backward inlet through the outlet boundary according to the analysis given in [3] or see its application in [29].

The inlet part of the boundary is formally divided into three disjoint parts: $\Gamma^{\mathrm{f}}_{\mathrm{in}} = \Gamma^{\mathrm{f}}_{\mathrm{in,dir}} \cup \Gamma^{\mathrm{f}}_{\mathrm{in,p}} \cup \Gamma^{\mathrm{f}}_{\mathrm{in},\varepsilon}$. The following boundary conditions are considered:

$$
\begin{aligned}
&\text{a)} \quad \mathbf{v}(x,t) = \mathbf{v}_{\mathrm{dir}}(x,t) && \text{for } x \in \Gamma^{\mathrm{f}}_{\mathrm{in,dir}},\\
&\text{b)} \quad (p(x,t) - p_{\mathrm{in}})\mathbf{n}^{\mathrm{f}} - \nu^{\mathrm{f}} \frac{\partial \mathbf{v}}{\partial \mathbf{n}^{\mathrm{f}}}(x,t) = -\frac{1}{2}\mathbf{v}(\mathbf{v}\cdot\mathbf{n}^{\mathrm{f}})^{-} && \text{for } x \in \Gamma^{\mathrm{f}}_{\mathrm{in,p}},\\
&\text{c)} \quad (p(x,t) - p_{\mathrm{in}})\mathbf{n}^{\mathrm{f}} - \nu^{\mathrm{f}} \frac{\partial \mathbf{v}}{\partial \mathbf{n}^{\mathrm{f}}}(x,t)\\
&\qquad\qquad = -\frac{1}{2}\mathbf{v}(\mathbf{v}\cdot\mathbf{n}^{\mathrm{f}})^{-} + \frac{1}{\varepsilon}(\mathbf{v} - \mathbf{v}_{\mathrm{dir}}) && \text{for } x \in \Gamma^{\mathrm{f}}_{\mathrm{in},\varepsilon}.
\end{aligned}
\tag{2.10}
$$

The choice of the inlet boundary condition is done by e.g. $\Gamma^{\mathrm{f}}_{\mathrm{in}} = \Gamma^{\mathrm{f}}_{\mathrm{in,dir}}$ and $\Gamma^{\mathrm{f}}_{\mathrm{in,p}} = \Gamma^{\mathrm{f}}_{\mathrm{in},\varepsilon} = \emptyset$. This notation facilitates the explanation of the weak formulation in the next section.

The conditions (2.10) represent three different mechanisms how the FSI is driven. The first is the classical Dirichlet boundary condition for inlet velocity. The second source of excitation can be given by the prescribed pressure difference Δp between the inlet $\Gamma^{\mathrm{f}}_{\mathrm{in}}$ and the outlet $\Gamma^{\mathrm{f}}_{\mathrm{out}}$ given by $\Delta p = p_{\mathrm{in}} - p_{\mathrm{ref}}$. The third boundary condition (2.10) c) is analogous to the first, i.e., it prescribes the inlet velocity $\mathbf{v}_{\mathrm{dir}}$ using the penalization approach, see [26]. In the presented study in condition (2.10) c) the inlet pressure p_{in} is taken as zero and ε is a suitable penalization parameter. The value of the parameter ε controls the switching between the Dirichlet boundary condition (limit $\varepsilon \to 0^{+}$) and the pressure drop boundary condition (limit $\varepsilon \to \infty$).

2.4. Coupling conditions. The fluid model (2.8) is coupled to the structure model (2.1) by using the kinematic and the dynamic boundary conditions prescribed at the common interface. Let us emphasize that the location of the common interface, which depends on the balance between the aerodynamic and the elastic forces, needs to be determined. Formally, the location is given with the use of the displacement $\mathbf{u}$ as

$$
\Gamma_{\mathrm{W}_t} = \{x \in \mathbb{R}^2;\ x = X + \mathbf{u}(X,t),\ X \in \Gamma_{\mathrm{W}_{\mathrm{ref}}}\}. \tag{2.11}
$$

For the fluid flow the boundary condition follows from the continuity of the fluid and the structural velocities on the interface Γ_{W_t}. Since the structure velocity $\partial\mathbf{u}/\partial t$ on the interface Γ_{W_t} is equal to the domain velocity $\mathbf{w}_D$, it has the form of the Dirichlet boundary condition (2.9) b).

For the elastic body the boundary condition is derived from the requirement of the stress continuity across the interface Γ_{W_t} in the normal direction. The prescribed

Neumann type of boundary condition has the form (2.4) d), where the vector $\mathbf{q}^{\mathrm{s}}$ reads

$$q_i^{\mathrm{s}}(X,t) = -\sum_{j=1}^{2} \sigma_{ij}^{\mathrm{f}}(x,t) n_j^{\mathrm{f}}(x,t), \quad x = X + \mathbf{u}(X,t),\ X \in \Gamma_{\mathrm{W}_{\mathrm{ref}}}, \tag{2.12}$$

and

$$\sigma_{ij}^{\mathrm{f}} = -\varrho^{\mathrm{f}} p \delta_{ij} + \varrho^{\mathrm{f}} \nu^{\mathrm{f}} \Big(\frac{\partial v_i}{\partial x_j} + \frac{\partial v_j}{\partial x_i} \Big)$$

are the components of the fluid stress tensor.

3. Numerical model

Both subproblems (2.1) and (2.8) are discretized in space by the FEM and in time by the finite difference method. For the time discretization the time interval $(0,T)$ is divided into n time steps $t_n = n\Delta t$. For the purpose of FEM the weak formulations of problems (2.1) and (2.8) are derived.

3.1. Elastic body. To achieve weak formulation the equation (2.1) is multiplied by a test function $\boldsymbol{\psi}$ and integrated over the whole domain Ω^{s}. The use of the Green theorem together with the boundary conditions (2.4) d) and the Hooke law (2.2) leads to the weak formulation

$$\Big(\varrho^{\mathrm{s}} \frac{\partial^2 \mathbf{u}}{\partial t^2}, \boldsymbol{\psi} \Big)_{\Omega^{\mathrm{s}}} + (\lambda^{\mathrm{s}} (\operatorname{div} \mathbf{u}) \mathbb{I} + 2\mu^{\mathrm{s}} \mathbf{e}^{\mathrm{s}}(\mathbf{u}), \mathbf{e}^{\mathrm{s}}(\boldsymbol{\psi}))_{\Omega^{\mathrm{s}}} = (\mathbf{f}^{\mathrm{s}}, \boldsymbol{\psi})_{\Omega^{\mathrm{s}}} + (\mathbf{q}^{\mathrm{s}}, \boldsymbol{\psi})_{\Gamma_{\mathrm{W}_{\mathrm{ref}}}}, \tag{3.1}$$

where the notation $(\cdot,\cdot)_{\mathcal{D}}$ means the dot product in the Lebesque spaces $L^2(\mathcal{D})$ or $\mathbf{L}^2(\mathcal{D})$ and the symbol $\mathbb{I}$ denotes the identity.

We say that $\mathbf{u} \in \mathbf{H}^1(\Omega^{\mathrm{s}})$ is a weak solution of equation (2.1) if it satisfies the boundary condition (2.4) c) and equation (3.1) holds for any test function $\boldsymbol{\psi} \in \mathbf{V}$, where $\mathbf{V} = \{\mathbf{f} \in \mathbf{H}^1(\Omega^{\mathrm{s}});\ \mathbf{f} = 0 \text{ on } \Gamma_{\mathrm{dir}}^{\mathrm{s}}\}$ and $\mathbf{H}^1(\Omega^{\mathrm{s}})$ is the vector Sobolev space. The solution $\mathbf{u} \in \mathbf{V}$ is then approximated by $\mathbf{u}_h$ using the finite dimensional subspace $\mathbf{V}_h$ of $\mathbf{V}$, i.e. $\mathbf{u}_h \in \mathbf{V}_h$. Using the standard base of the piecewise linear finite element space, the system (3.1) is transformed to the system

$$\mathbb{M}\ddot{\boldsymbol{\alpha}} + \mathbb{C}\dot{\boldsymbol{\alpha}} + \mathbb{K}\boldsymbol{\alpha} = \mathbf{b}(t), \tag{3.2}$$

where $\mathbb{M}$ denotes the mass matrix, $\mathbb{K}$ denotes the stiffness matrix, $\mathbb{C}$ is the artificially added damping matrix, see e.g. [28], further $\mathbf{b}(t)$ denotes the load vector and the vector $\boldsymbol{\alpha}$ consists of the displacements of the mesh vertices for the used P1-finite element space.

For the structure model the proportional damping is used, i.e. the matrix $\mathbb{C}$ is chosen in the form $\mathbb{C} = c_1\mathbb{M} + c_2\mathbb{K}$, where the parameters c_1, c_2 are chosen in such a way that the whole elastic system is relatively weakly damped (for frequencies in the neighbourhood of the first two eigenfrequencies), see [16] or [32].

System (3.2) is time discretized with the aid of the Newmark method, see e.g. [4] or [10].

3.2. Fluid flow. The procedure for numerical solution of the fluid flow problem is more difficult. First the problem (2.8) is discretized in time by the backward difference formula of the second order (BDF2)

$$\frac{D^A\mathbf{v}}{Dt}(t_{n+1}) \approx \frac{3\mathbf{v}^{n+1} - 4\overline{\mathbf{v}}^n + \overline{\mathbf{v}}^{n-1}}{2\Delta t}, \tag{3.3}$$

where for a fixed time instant t_{n+1} we denote $\overline{\mathbf{v}}^i(x) = \mathbf{v}^i(\tilde{x})$ for $\tilde{x} = A_{t_i}(A^{-1}_{t_{n+1}}(x))$, $i \in \{n-1, n\}$ and $x \in \Omega^{\mathrm{f}}_{t_{n+1}}$. For the sake of simplicity in the next sections we omit the time index $n+1$, set $\Omega^{\mathrm{f}} := \Omega^{\mathrm{f}}_{t_{n+1}}$ and use the notation $\Gamma^{\mathrm{f}}_{\mathrm{in,p}\cup\varepsilon} = \Gamma^{\mathrm{f}}_{\mathrm{in,p}} \cup \Gamma^{\mathrm{f}}_{\mathrm{in},\varepsilon}$.

First the space $\mathbf{X} = X_1 \times X_2$ is defined as $X_1 = X = \{f \in H^1(\Omega^{\mathrm{f}});\ f = 0 \text{ on } \Gamma^{\mathrm{f}}_{\mathrm{dir}} \cup \Gamma^{\mathrm{f}}_{\mathrm{in,dir}} \cup \Gamma^{\mathrm{f}}_{\mathrm{W}_{t_{n+1}}}\} \subset H^1(\Omega^{\mathrm{f}})$, $X_2 = \{f \in X;\ f = 0 \text{ on } \Gamma^{\mathrm{f}}_{\mathrm{sym}}\}$ and $M = L^2(\Omega^{\mathrm{f}})$. Next, in order to obtain the weak formulation of the flow problem in space the two equations of (2.8) are multiplied by test functions $\boldsymbol{\varphi} \in \mathbf{X}$ and $q \in M$, respectively, integrated over the whole fluid domain Ω^{f}, summed up, and the Green theorem is applied to pressure and viscous terms. This leads to the equation

$$\begin{aligned}\Big(\frac{3\mathbf{v}}{2\Delta t}, \boldsymbol{\varphi}\Big)_{\Omega^{\mathrm{f}}} + (((\mathbf{v} - \mathbf{w}_D)\cdot\nabla)\mathbf{v}, \boldsymbol{\varphi})_{\Omega^{\mathrm{f}}} + \nu^{\mathrm{f}}(\nabla\mathbf{v}, \nabla\boldsymbol{\varphi})_{\Omega^{\mathrm{f}}} - (p, \operatorname{div}\boldsymbol{\varphi})_{\Omega^{\mathrm{f}}} \\ + (q, \operatorname{div}\mathbf{v})_{\Omega^{\mathrm{f}}} = \Big(\frac{4\overline{\mathbf{v}}^n - \overline{\mathbf{v}}^{n-1}}{2\Delta t}, \boldsymbol{\varphi}\Big)_{\Omega^{\mathrm{f}}} + \Big(\nu^{\mathrm{f}}\frac{\partial\mathbf{v}}{\partial\mathbf{n}^{\mathrm{f}}} - p\mathbf{n}^{\mathrm{f}}, \boldsymbol{\varphi}\Big)_{\partial\Omega^{\mathrm{f}}}\end{aligned} \tag{3.4}$$

Let us mention that the classical do-nothing boundary condition follows from setting the last term of (3.4) equal to a constant, see e.g. [13]. In order to avoid the possible instability due to the back inflow at the outlet part of the boundary, the convective term is further reformulated as

$$\begin{aligned}(((\mathbf{v} - \mathbf{w}_D)\cdot\nabla)\mathbf{v}, \boldsymbol{\varphi})_{\Omega^{\mathrm{f}}} = \frac{1}{2}(((\mathbf{v} - 2\mathbf{w}_D)\cdot\nabla)\mathbf{v}, \boldsymbol{\varphi})_{\Omega^{\mathrm{f}}} - \frac{1}{2}((\mathbf{v}\cdot\nabla)\boldsymbol{\varphi}, \mathbf{v})_{\Omega^{\mathrm{f}}} \\ + \frac{1}{2}((\mathbf{v}\cdot\mathbf{n})^+\mathbf{v}, \boldsymbol{\varphi})_{\partial\Omega^{\mathrm{f}}} + \frac{1}{2}((\mathbf{v}\cdot\mathbf{n})^-\mathbf{v}, \boldsymbol{\varphi})_{\partial\Omega^{\mathrm{f}}},\end{aligned} \tag{3.5}$$

where $(\alpha)^+$ denotes the positive part of a real number α, defined as $(\alpha)^+ = \max\{0, \alpha\}$. The last two terms of (3.5) and the last term of (3.4) are nonzero only at the boundaries $\Gamma^{\mathrm{f}}_{\mathrm{out}}$, $\Gamma^{\mathrm{f}}_{\mathrm{in,p}}$ and $\Gamma^{\mathrm{f}}_{\mathrm{in},\varepsilon}$ due to the definition of the space $\mathbf{X}$.

The boundary terms over $\Gamma^{\mathrm{f}}_{\mathrm{out}}$ in equations (3.4) and (3.5) motivate the specification of the outlet boundary condition (2.9) d), where p_{ref} is the reference pressure prescribed at $\Gamma^{\mathrm{f}}_{\mathrm{out}}$.

The inlet boundary condition prescribed at $\Gamma^{\mathrm{f}}_{\mathrm{in,p}}$ is derived in the same way except denoting the pressure constant by p_{in}, which leads to boundary condition (2.10) b). The formulation of boundary condition (2.10) c) on $\Gamma^{\mathrm{f}}_{\mathrm{in},\varepsilon}$ follows the same procedure with the reference pressure set $p_{\mathrm{in}} = 0$ and the added term $\frac{1}{\varepsilon}(\mathbf{v} - \mathbf{v}_{\mathrm{dir}}, \boldsymbol{\varphi})_{\Gamma^{\mathrm{f}}_{\mathrm{in},\varepsilon}}$.

Finally, we introduce a trilinear form $a(\cdot;\cdot,\cdot)$ with arguments $V^* = (\mathbf{v}^*, p^*)$, $V = (\mathbf{v}, p)$ and $\Phi = (\boldsymbol{\varphi}, q)$ by

$$
\begin{aligned}
(3.6)\quad a(V^*; V, \Phi) = {} & \Big(\frac{3\mathbf{v}}{2\Delta t}, \boldsymbol{\varphi}\Big)_{\Omega^{\mathrm{f}}} + \frac{1}{2}(((\mathbf{v}^* - 2\mathbf{w}_D)\cdot\nabla)\mathbf{v}, \boldsymbol{\varphi})_{\Omega^{\mathrm{f}}} - \frac{1}{2}((\mathbf{v}^*\cdot\nabla)\boldsymbol{\varphi}, \mathbf{v})_{\Omega^{\mathrm{f}}} \\
& + \frac{1}{2}((\mathbf{v}^*\cdot\mathbf{n})^+\mathbf{v}, \boldsymbol{\varphi})_{\Gamma^{\mathrm{f}}_{\mathrm{out}}} + \nu^{\mathrm{f}}(\nabla\mathbf{v}, \nabla\boldsymbol{\varphi})_{\Omega^{\mathrm{f}}} - (p, \operatorname{div}\boldsymbol{\varphi})_{\Omega^{\mathrm{f}}} \\
& + (q, \operatorname{div}\mathbf{v})_{\Omega^{\mathrm{f}}} + \frac{1}{2}((\mathbf{v}^*\cdot\mathbf{n})^+\mathbf{v}, \boldsymbol{\varphi})_{\Gamma^{\mathrm{f}}_{\mathrm{in,p}\cup\varepsilon}} + \frac{1}{\varepsilon}(\mathbf{v}, \boldsymbol{\varphi})_{\Gamma^{\mathrm{f}}_{\mathrm{in},\varepsilon}}
\end{aligned}
$$

and a linear functional $f(\cdot)$ by

$$
\begin{aligned}
(3.7)\qquad f(\Phi) = {} & \Big(\frac{4\overline{\mathbf{v}}^n - \overline{\mathbf{v}}^{n-1}}{2\Delta t}, \boldsymbol{\varphi}\Big)_{\Omega^{\mathrm{f}}} + (p_{\mathrm{ref}}\mathbf{n}^{\mathrm{f}}, \boldsymbol{\varphi})_{\Gamma^{\mathrm{f}}_{\mathrm{out}}} \\
& + (p_{\mathrm{in}}\mathbf{n}^{\mathrm{f}}, \boldsymbol{\varphi})_{\Gamma^{\mathrm{f}}_{\mathrm{in,p}\cup\varepsilon}} + \frac{1}{\varepsilon}(\mathbf{v}_{\mathrm{dir}}, \boldsymbol{\varphi})_{\Gamma^{\mathrm{f}}_{\mathrm{in},\varepsilon}}.
\end{aligned}
$$

In practice only one of the sets $\Gamma^{\mathrm{f}}_{\mathrm{in,dir}}$, $\Gamma^{\mathrm{f}}_{\mathrm{in,p}}$, $\Gamma^{\mathrm{f}}_{\mathrm{in},\varepsilon}$ is allowed to be nonempty leading to significant reduction of boundary terms in (3.6) and (3.7).

Then the weak formulation of equation (2.8) at time t_{n+1} can be defined as the problem to find $V = (\mathbf{v}, p) \in \mathbf{H}^1(\Omega^{\mathrm{f}}) \times M$ such that $\mathbf{v}$ satisfies boundary conditions (2.9) a), b), c1) and (2.10) a) and equation

$$
(3.8)\qquad a(V; V, \Phi) = f(\Phi)
$$

holds for any $\Phi = (\boldsymbol{\varphi}, q) \in \mathbf{X} \times M$.

3.2.1. Numerical approximation and stabilization. In order to approximate the solution V, the velocity and the pressure spaces $\mathbf{X}$ and M are approximated by the FE subspaces $\mathbf{X}_h = \mathbf{W}_h \cap \mathbf{X}$ and $M_h \subset M$, which satisfy the Babuška–Brezzi inf-sup condition, see e.g. [13]. For practical computation the P1-bubble/P1 finite elements were chosen, see [13], which means that $\mathbf{W}_h = \{f_i \in C(\overline{\Omega^{\mathrm{f}}});\ \mathbf{f} = 0 \text{ on } \Gamma^{\mathrm{f}}_{\mathrm{dir}},\ f_i|_K \in \mathbb{P}_1^{\mathrm{bub}}(K) \text{ for all } K \in \mathcal{T}^{\mathrm{f}}_h\}$ and $M_h = \{f \in C(\overline{\Omega^{\mathrm{f}}});\ f|_K \in \mathbb{P}_1(K) \text{ for all } K \in \mathcal{T}^{\mathrm{f}}_h\}$, where $\mathcal{T}^{\mathrm{f}}_h$ is a regular, admissible triangulation of the domain Ω^{f}, $\mathbb{P}_1(K)$ is the space of polynomials of the

first order on the set K and the space $\mathbb{P}_1^{\mathrm{bub}}(K) = \mathbb{P}_1(K) \cup \{\boldsymbol{\varphi}_{\mathrm{bub}}\}$ is the $\mathbb{P}_1$ space enriched by the cubic bubble function $\boldsymbol{\varphi}_{\mathrm{bub}}$.

The FE solution can be numerically unstable in the case of high Reynolds number flows, when the convection dominates. This is principally caused by the unresolved velocity gradients due to a too coarse grid. The regions with unresolved high velocity gradients can be characterized by high values of local Reynold number Re_K, defined later.

The applied residual based stabilization consists in the additional testing of equations (2.8) by gradients of test functions in the streamline direction. This approach in comparison with other methods like e.g. artificial diffusion or local projection methods enables to achieve stable discretization, which is consistent, high-order and introduces less numerical diffusion, see e.g. [18], [12].

The stabilization is realized by adding stabilizing terms to the equation (3.8). These terms are defined for any $V^* = (\mathbf{v}^*, p^*) \in \mathbf{W}_h \times M_h$, $V = (\mathbf{v}, p) \in \mathbf{W}_h \times M_h$ and $\Phi = (\boldsymbol{\varphi}, q) \in \mathbf{X}_h \times M_h$ as

$$
\begin{aligned}
(3.9) \qquad L_h(V^*; V, \Phi) &= \sum_{K \in \mathcal{T}_h} \delta_K \Big(\frac{3\mathbf{v}}{2\Delta t} + ((\mathbf{v}^* - \mathbf{w}_D) \cdot \nabla)\mathbf{v} \\
&\qquad + \nabla p - \nu^{\mathrm{f}} \Delta \mathbf{v}, ((\mathbf{v}^* - \mathbf{w}_D) \cdot \nabla)\boldsymbol{\varphi} \Big)_K, \\
P_h(V^*; V, \Phi) &= \sum_{K \in \mathcal{T}_h} \delta_K \Big(\frac{3\mathbf{v}}{2\Delta t} + ((\mathbf{v}^* - \mathbf{w}_D) \cdot \nabla)\mathbf{v} + \nabla p - \nu^{\mathrm{f}} \Delta \mathbf{v}, \nabla q \Big)_K, \\
D_h(V, \Phi) &= \sum_{K \in \mathcal{T}_h} \tau_K (\operatorname{div} \mathbf{v}, \operatorname{div} \boldsymbol{\varphi})_K
\end{aligned}
$$

and

$$
\begin{aligned}
(3.10) \qquad F_h(V^*; \Phi) &= \sum_{K \in \mathcal{T}_h} \delta_K \Big(\frac{4\overline{\mathbf{v}}^n - \overline{\mathbf{v}}^{n-1}}{2\Delta t}, \ ((\mathbf{v}^* - \mathbf{w}_D) \cdot \nabla)\boldsymbol{\varphi} \Big)_K, \\
G_h(\Phi) &= \sum_{K \in \mathcal{T}_h} \delta_K \Big(\frac{4\overline{\mathbf{v}}^n - \overline{\mathbf{v}}^{n-1}}{2\Delta t}, \nabla q \Big)_K,
\end{aligned}
$$

where the parameters $\tau_K = \tau_K(V^*)$ and $\delta_K = \delta_K(V^*)$ are locally defined by

$$
(3.11) \qquad \tau_K = \nu^{\mathrm{f}} \Big(1 + \mathrm{Re}_K + 2 \frac{h_K^2}{\nu^{\mathrm{f}} \Delta t} \Big), \quad \delta_K = \frac{h_K^2}{\tau_K}.
$$

The local Reynold number Re_K is set to $\mathrm{Re}_K = (h_K \|\mathbf{v}^* - \mathbf{w}_D\|_K)/2\nu^{\mathrm{f}}$ and the local element length h_K is taken as square root of the triangle area K, see [10].

The stabilized problem (3.8) reads: Find a function pair $V_h = (\mathbf{v}_h, p_h) \in \mathbf{W}_h \times M_h$ such that $\mathbf{v}_h$ satisfies the boundary conditions (2.9) a), b), c) and (2.10) a), and

$$a(V_h; V_h, \Phi_h) + L_h(V_h; V_h, \Phi_h) + P_h(V_h; V_h, \Phi_h) + D_h(V_h, \Phi_h) = f(\Phi_h) + F_h(V_h; \Phi_h) + G_h(\Phi_h), \tag{3.12}$$

holds for any test functions $\Phi_h = (\boldsymbol{\varphi}_h, q_h) \in \mathbf{X}_h \times M_h$.

The used stabilization combines the SUPG, the PSPG and 'div-div' stabilization methods. The SUPG method corresponds to forms L_h and F_h, the PSPG method is realized through the form P_h and the functional G_h and finally the so-called 'div-div' stabilization enforces (better) fulfilment of continuity equation by the inclusion of the additional form D_h into equation (3.12).

3.2.2. Linearization. The system of equations (3.12) is nonlinear and is solved by fixed point iteration. Starting from an initial estimate V_h^0 and for $j = 0, 1, 2, \ldots$ we seek $V_h^{j+1} = (\mathbf{v}_h^{\bullet,j+1}, p_h^{\bullet,j+1}) \in \mathbf{W}_h \times M_h$ such that $\mathbf{v}_h^{\bullet,j+1}$ satisfies the boundary conditions (2.9) a), b), c1) and (2.10) a), and the equation

$$a(V_h^j; V_h^{j+1}, \Phi_h) + L_h(V_h^j; V_h^{j+1}, \Phi_h) + P_h(V_h^j; V_h^{j+1}, \Phi_h) + D_h(V_h^{j+1}, \Phi_h) = f(\Phi_h) + F_h(V_h^j; \Phi_h) + G_h(\Phi_h) \tag{3.13}$$

holds for any $\Phi_h \in \mathbf{X}_h \times M_h$. The process is repeated until the convergence criterion $\|V_h^{j+1} - V_h^j\| < \varepsilon^{\mathrm{f}}$ is reached. For the solution of the linear system (3.13) the mathematical library UMFPACK is employed, see [6].

3.3. Construction of ALE mapping. The ALE mapping A_t should provide a smooth mapping $\Omega_{\mathrm{ref}}^{\mathrm{f}}$ onto Ω_t^{f} for any $t \in (0, T)$, which is quite robust, easy to implement and capable of handling very complex domain deformation. These requirements are fulfilled by the pseudo-elastic approach, see e.g. [20]. Here, the approximation of the ALE mapping is constructed at time instant t_n.

The pseudo-elastic approach seeks the solution of an artificial stationary elasticity problem on $\Omega_{\mathrm{ref}}^{\mathrm{f}}$ with known deformation of the boundary $\partial\Omega_{\mathrm{ref}}^{\mathrm{f}}$. The sought displacement $\mathbf{d} = (d_1, d_2)$ describes the displacement of any point $X \in \Omega_{\mathrm{ref}}^{\mathrm{f}}$ and similarly to problem (2.1) we solve the equation

$$\frac{\partial \tau_{ij}^{\mathrm{ale}}}{\partial X_j} = 0 \tag{3.14}$$

in $\Omega_{\mathrm{ref}}^{\mathrm{f}}$ together with the boundary conditions

$$\mathbf{d} = \mathbf{0} \quad \text{on } \Gamma_{\mathrm{dir}}^{\mathrm{f}} \cup \Gamma_{\mathrm{in}}^{\mathrm{f}} \cup \Gamma_{\mathrm{out}}^{\mathrm{f}}, \quad \mathbf{d} = \mathbf{u}(t_n) \quad \text{on } \Gamma_{\mathrm{W}t_n}^{\mathrm{f}}, \qquad \mathbf{d} \cdot \mathbf{n}^{\mathrm{f}} = 0, \quad \mathbf{t}^{\mathrm{f}} \cdot \boldsymbol{\tau}^{\mathrm{ale}} \cdot \mathbf{n}^{\mathrm{f}} = 0 \quad \text{on } \Gamma_{\mathrm{sym}}^{\mathrm{f}}. \tag{3.15}$$

Here, $\tau_{ij}^{\mathrm{ale}} = \lambda^{\mathrm{ale}}(\operatorname{div}\mathbf{d})\delta_{ij} + 2\mu^{\mathrm{ale}} e_{ij}^{\mathrm{s}}(\mathbf{d})$ and $\lambda^{\mathrm{ale}}, \mu^{\mathrm{ale}}$ are artificial Lamé coefficients. Let us emphasize that for the boundary $\Gamma_{\mathrm{sym}}^{\mathrm{f}}$ it was found to be of significant advantage to prescribe only the normal component of the displacement and to keep the tangential one free. This condition allows to handle substantially larger fluid mesh deformation introduced by large elastic body displacements.

Similarly to paragraph 3.1 the system of equations (3.14) is weakly formulated and the displacement $\mathbf{d}$ is approximated by $\mathbf{d}_h$ taken as a linear combination of the basis functions. The same discretization procedure based on the FEM as described in paragraph 3.1 leads to the system

$$\mathbb{K}^{\mathrm{ale}}\boldsymbol{\alpha}^{\mathrm{ale}} = \mathbf{0}, \tag{3.16}$$

where $\mathbb{K}^{\mathrm{ale}}$ is the stiffness matrix and the components of the vector $\boldsymbol{\alpha}^{\mathrm{ale}}$ are the values of the displacement $\mathbf{d}$ at mesh vertices (for the used first order Lagrange finite elements). The domain velocity $\mathbf{w}_{D,h}(t_n)$ is approximated by using the BDF2 formula, see [10].

3.4. Coupling algorithm. The strong coupling algorithm is applied to the solution of the FSI problem, see [10]. It means that for each time step we solve the flow and structure problems iteratively, see Figure 2, until the convergence criterion

$$\|\mathbf{q}^{s,l+1} - \mathbf{q}^{s,l}\| < \varepsilon^{\mathrm{FSI}}, \tag{3.17}$$

is met where the upper index l denotes the inner iteration number; for more details see [28]. The algorithm performs usually 3–8 inner loops for chosen $\varepsilon^{\mathrm{FSI}} = 10^{-3}$.

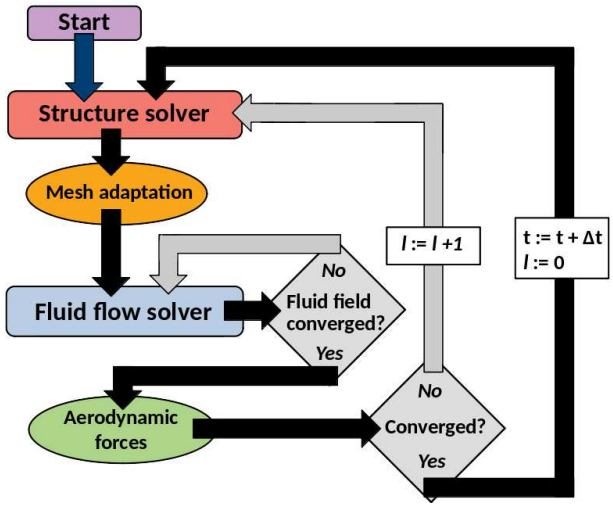

Figure 2. Diagram showing the consequent steps of FSI algorithm with inner cycles and implemented strong coupling.

4. Numerical results

All results of numerical simulation are achieved with the following setting. The constant time step Δt was chosen as $2.5 \cdot 10^{-5}$ s. The densities $\varrho^{\mathrm{s}} = 1000\,\mathrm{kg/m^3}$, $\varrho^{\mathrm{f}} = 1.185\,\mathrm{kg/m^3}$ and the kinematic viscosity $\nu^{\mathrm{f}} = 1.47 \cdot 10^{-5}\,\mathrm{m^2/s}$ were set. The Young modulus and the Poisson ratio were chosen as $E^{\mathrm{s}} = 8\,\mathrm{kPa}$ and $\sigma^{\mathrm{s}} = 0.4$, respectively. The damping parameters were determined as $c_1 = 5\,\mathrm{s}^{-1}$, $c_2 = 2.0 \cdot 10^{-5}\,\mathrm{s}$.

The reference shape of the elastic body depicted in Figure 3 was taken from the article [26], where the body is a simplified model of the human vocal fold in a glottal channel, see [15], [16], [17]. The FSI model was for the sake of simplicity considered as symmetric with symmetry axis $y = 0$. The half-gap $g_0(t)$, which denotes the distance between the top of the elastic body and the symmetry axis of the channel, was initially set as $g_{\mathrm{init}} = 0.4\,\mathrm{mm}$. Further, at the top of the elastic body the sensor S is located having the coordinates $[4.99, -0.505]$ mm in the reference domain.

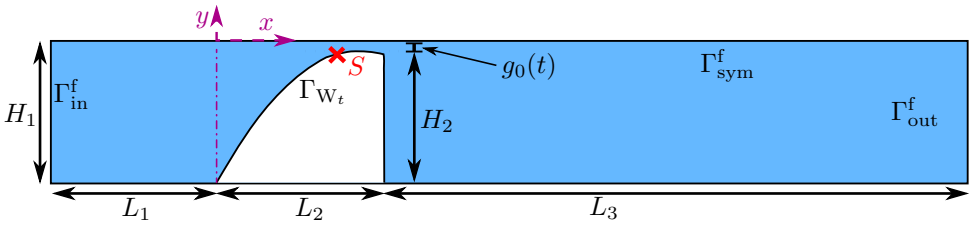

Figure 3. The FSI domains with marked boundaries and half-gap distance $g_0(t)$ and point S. The considered highlighted dimensions are: $H_1 = 5.8\,\mathrm{mm}$, $H_2 = 5.4\,\mathrm{mm}$, $g_0(0) = 0.4\mathrm{mm}$, $L_1 = 6.8\,\mathrm{mm}$, $L_2 = 6.8\,\mathrm{mm}$ and $L_3 = 23.8\,\mathrm{mm}$.

The results of numerical simulations are divided into two sections. In the first section the influence of inlet boundary conditions on the pressure and velocity fluctuations at the channel inlet is investigated and the parametric study, studying the influence of the penalization parameter on the FSI process, is performed. In the second section the flow-induced vocal folds vibrations in the unstable regime are shown.

4.1. Effect of the inlet boundary conditions on flow characteristics. This section consists of three paragraphs. In the first the prescribed periodic motion of the elastic wall is studied. The second paragraph is devoted to the parametric study, while in the third the full FSI interaction is simulated.

4.1.1. Prescribed motion of structure. First, the performance of the considered boundary condition was tested for the case of prescribed vibrations of the vocal

fold model. The displacement of the point $[x, y] \in \Omega^s$ of the elastic body Ω^s at time $t \in [0, T]$ was prescribed as

$$u_1(x, y, t) = 0, \quad u_2(x, y, t) = \frac{C_{\text{driven}}}{100} \cdot (y + g_0 + H_2) \cdot \sin(2\pi f_{\text{driven}} t), \tag{4.1}$$

where $C_{\text{driven}}, f_{\text{driven}}$ are given parameters and $g_0 + H_2 = 0.0058\,\text{m}$. The influence of the vibrating elastic body with $f_{\text{driven}} = 100\,\text{Hz}$ on the flow field without any interaction was considered. This prescribed motion of the elastic body enables to close the channel up to the minimal half-gap $g_{\min} = 0.0114\,\text{mm}$ for setting $C_{\text{driven}} = 7.2$, in what follows denoted as the reference driven mode.

Three different scenarios with different inlet boundary conditions were simulated: the Dirichlet boundary condition (2.10) a) with prescribed inlet velocity referenced as "vel", the case with the prescribed pressure drop by condition (2.10) b) labeled as "pres" and the case of penalization boundary condition (2.10) c) denoted as "pen". The used parameters were $\mathbf{v}_{\text{dir}} = (1.7, 0)\,\text{m/s}$, $\varepsilon = \frac{1}{2000}\,\text{s/m}$ and $\Delta p = 400\,\text{Pa}$.

The results in terms of the inlet quantities are shown in Figure 4. The time behaviour of the average inlet flow velocity reveals the expected different behaviour in three studied cases, the inlet velocity being constant for the case "vel" and oscillating for the case "pres" around its mean value (approximately the same as for "vel"). In the "pen" case the inlet velocity for the maximally open channel is almost the same as for the case "vel", but during the channel closing it rapidly drops near to zero (similarly to the "pres" case).

In the case "pres" the pressure drop is almost constant, while for the case "vel" the pressure grows fast during the channel closing. For the limit case of the completely closed channel, the theoretical value of pressure drop will reach infinity. In the case "pen" pressure drop remains bounded with reasonable amplitude comparable with experiments, see [14]. The maximal value of pressure drop is below referred as pressure peak.

In the case "pen" the velocity magnitude distribution is shown in Figure 5. It can be noticed that during the channel closing the velocity magnitude is decreasing, which is in contrary to the behaviour in the case "vel", where based on the continuity equation the local velocity theoretically tends to infinity. In the case "pen", the maximal velocity in the narrowest part of the channel for the time instant of minimal half-gap $g_0 = g_{\min}$ equals 25.0 m/s which is comparable with the maximal velocity 28.9 m/s for the time instant when the half-gap $g_0(t)$ equals the initial half-gap $g_{\text{ini}} = 0.4\,\text{mm}$. On the other hand, for the case "vel" the maximal velocity in the narrowest part of the channel for the time instant of minimal half-gap exceeds an unreal value of cca 300 m/s.

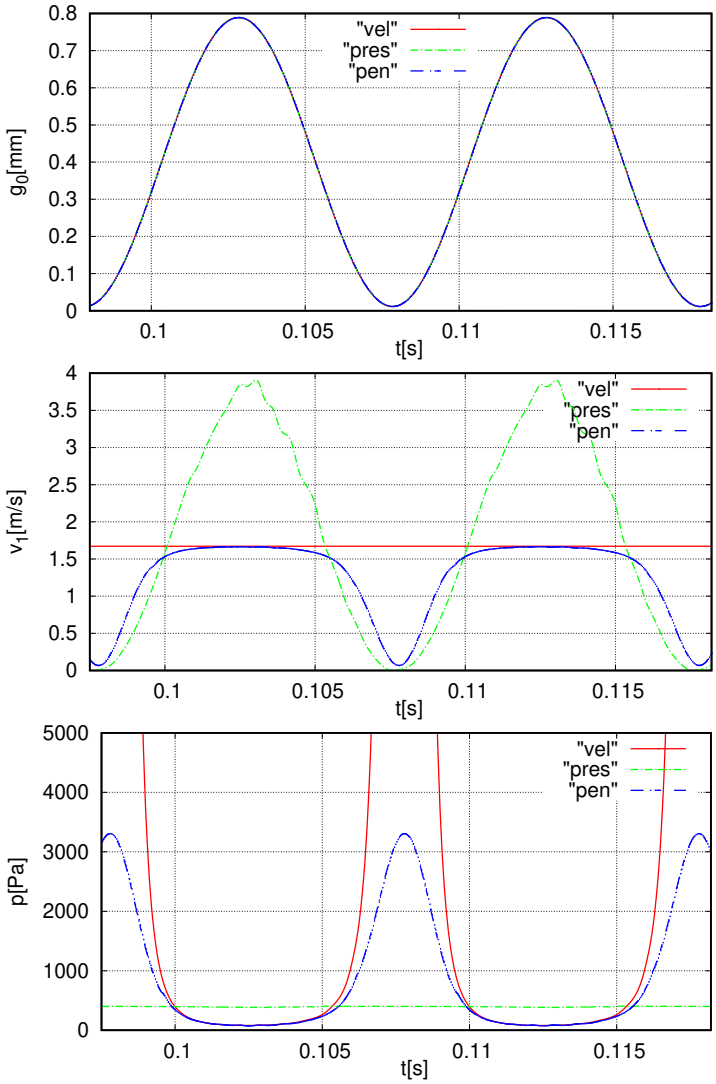

Figure 4. The top figure shows the prescribed half-gap in dependence on time t with its minimum $g_{\min}$, the middle figure shows the inlet velocity in dependence on time for the three types of the used inlet boundary conditions. The bottom figure presents a detail of the pressure drop during two periods of the prescribed motion.

4.1.2. Parametric study of an optimal value of the penalty parameter. First, the sensitivity of the flow field characteristics to the changes of the penalization parameter were tested for the reference prescribed motion of the structure as in paragraph 4.1.1. The dependence of the pressure peaks on the penalization parameter ε is shown in Figure 6, which presents also the dependence of the maximal, the

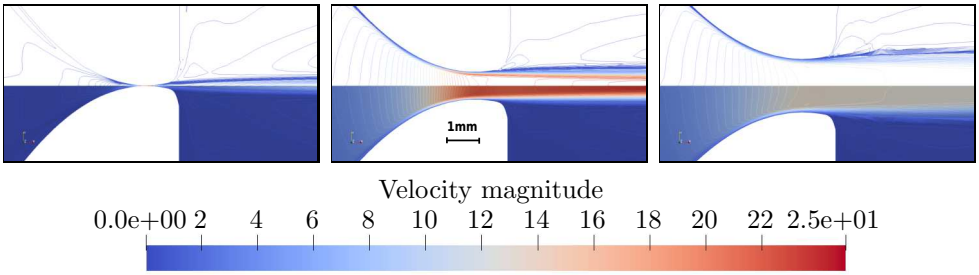

Figure 5. The magnitude of the flow velocity distribution around the vibrating structure at three time instants for the case "pen". Left picture shows the moment with minimal half-gap $g_{\min}$, middle one with the initial (mean) half-gap and the right picture depicts the moment with maximally open channel. The scale of velocity contours is common for all three pictures.

average and the minimal flow rate Q on the parameter ε. The most rapid changes occur for the penalization parameter in the range $10^{-6}\,\mathrm{s/m} - 10^{-4}\,\mathrm{s/m}$, where the pressure peaks demonstrate a steep decrease from its maximum to minimum and the average flow rate is still close to its maximum.

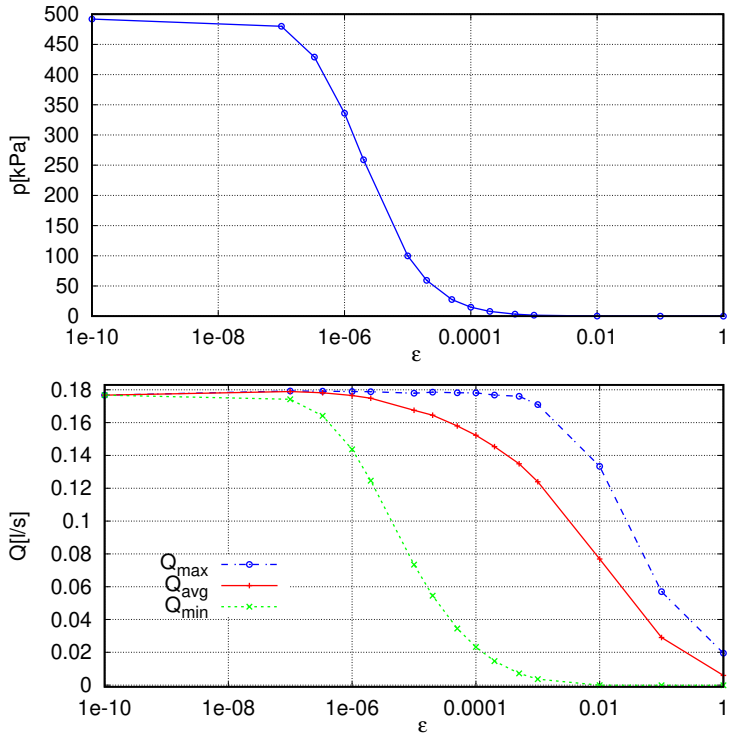

Figure 6. The dependence of pressure peaks and the inlet flow rate on the penalization parameter ε is plotted at the top and at the bottom, respectively.

The flow characteristics are quite sensitive to the prescribed minimal half-gap, as expected. The sensitivity of the flow field in the channel was tested on a series of simulations with the prescribed motion of the structure given by the formula (4.1) with the values of $C_{\mathrm{driven}} \in \{6.0, 7.0, 7.2, 7.28\}$. The top graph in Figure 7 shows the dependence of the maximal pressure peaks (compare with Figure 4) on the gradually decreasing minimal value of the half-gap to $g_0(t_{\min}) = 0.0071\,\mathrm{mm}$ corresponding to $C_{\mathrm{driven}} = 7.28$. The bottom graph reports the dependence of the average flow rate evaluated in the channel inlet on the minimal half-gap. In both the graphs, the results obtained for the same value of the penalization parameter ε and connected with a line represent actually ε-isocurves. The interesting part is near $g_0 \to 0$, where the line of the maximal pressure difference decreases gradually, i.e. the pressure peaks grow faster for small values of ε, imitating the Dirichlet boundary condition, while the average flow rate does not depend on the minimal half-gap in this range of the parameter ε.

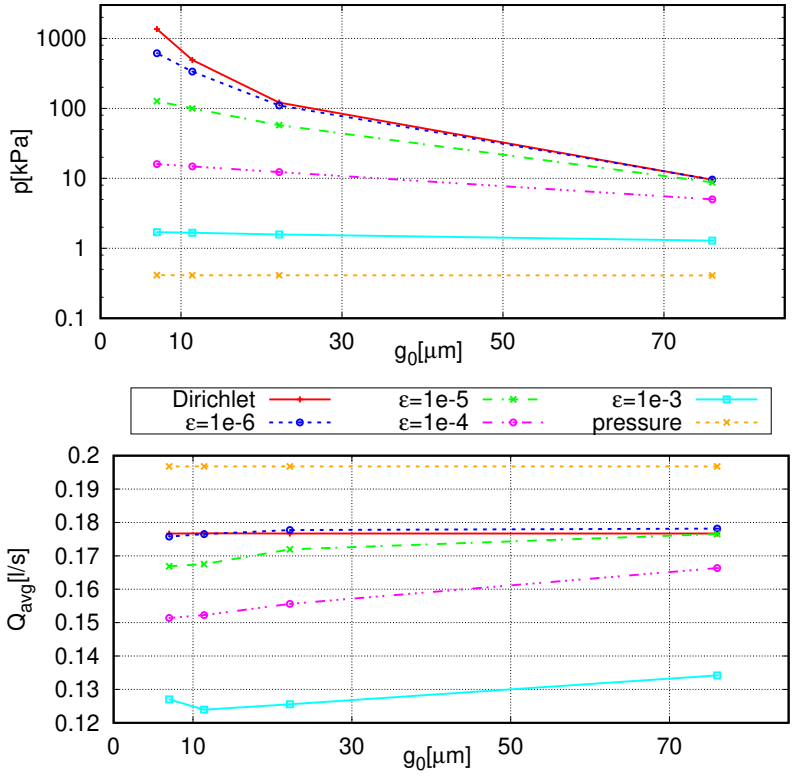

Figure 7. Computed isocurves of ε for penalty approach together with results for two cases of classic inlet boundary conditions shown in the graphs, where the dependence of pressure peaks and average flow rate on the minimal half-gap is plotted.

The graphs in Figures 6 and 7 allow to estimate the suitable value of penalization parameter according to measured or expected pressure and flow rate values relevant to similar FSI problems. The described technique how to choose the penalization parameter ε is applicable in a more general case.

4.1.3. Fluid-structure interaction. From this point further the full FSI problem is numerically solved. In order to ensure the half-gap between the channel walls to be consistent and comparable with the previous numerical results [26] or [17], the static force supporting the elastic structure is eliminated from the dynamic response of the structure. The static force $\mathbf{q}^{\mathrm{s}}_{\mathrm{stat}}$ is computed from the numerical solution of the flow field $\mathbf{q}^{\mathrm{s}}_{\mathrm{stat}}(X) := \mathbf{q}^{\mathrm{s}}(X, t_{\mathrm{release}})$ at the chosen time instant $t_{\mathrm{release}} > 0$ using the static channel configuration. Here, t_{release} is chosen to be such a time that the fluid transitional effects almost completely disappear. Then for $t > t_{\mathrm{release}}$ the interaction is switched on with the modified aerodynamic force

$$\mathbf{q}^{\mathrm{s}}_{\mathrm{mod}}(X, t) = \mathbf{q}^{\mathrm{s}}(X, t) - \mathbf{q}^{\mathrm{s}}_{\mathrm{stat}}(X). \tag{4.2}$$

The modified aerodynamic force $\mathbf{q}^{\mathrm{s}}_{\mathrm{mod}}$ has actually the meaning of force fluctuations around the new equilibrium position equal to the original initial half-gap position. If the static force were not imposed, the equilibrium half-gap would be different and results would not be comparable with the reference results.

The influence of the inlet boundary conditions (2.10) in the case of full interaction is studied for inlet velocity prescribed by the condition (2.10) a) or (2.10) c) denoted further as "vel" or "pen" case, respectively. The case of the applied condition (2.10) b) is labeled again as "pres". The inlet velocity was given as $\mathbf{v}_{\mathrm{dir}} = (1.9, 0.0)\,\mathrm{m/s}$ and the penalization parameter was set to $\varepsilon = 10^{-5}\,\mathrm{s/m}$ as in the simulation considered in [26]. The chosen pressure drop $\Delta p = p_{\mathrm{ref}} - 0 = 450\,\mathrm{Pa}$ in the "pres" case slightly overestimates the computed pressure difference in the "vel" case.

The elastic channel walls were released for the interaction after 0.035 s of the simulation, when the flow field was already fully developed and the static force $\mathbf{q}^{\mathrm{s}}_{\mathrm{stat}}$ was determined. Then the full interaction procedure started.

Figure 8 shows the different behaviour of the airflow velocity at the inlet boundary $\Gamma^{\mathrm{f}}_{\mathrm{in}}$. The classic Dirichlet boundary conditions (2.10) a) keep the inlet velocity constant, while the pressure difference prescribed by condition (2.10) c) leads to oscillating inlet velocity with fast growing of the amplitude. The inlet velocity in the case of penalization approach given by (2.10) b) has an oscillating character with small amplitudes around a slightly lower average value than in the case with the Dirichlet condition.

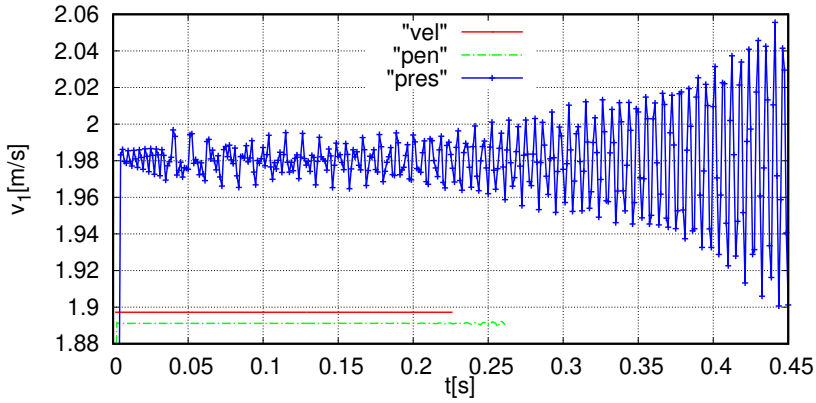

Figure 8. Average inlet velocity for cases "vel", "pen" and "pres".

The corresponding results computed for the pressure difference Δp between the inlet $\Gamma^{\mathrm{f}}_{\mathrm{in}}$ and the outlet $\Gamma^{\mathrm{f}}_{\mathrm{out}}$ are displayed in Figure 9. The pressure difference in the case "pres" is almost constant. For the prescribed inlet velocity in cases "vel" and "pen" the pressure difference shows significant oscillating behaviour connected with the increasing channel walls vibration amplitude, see Figure 10. For the penalization approach the pressure drop oscillation is delayed similarly to the channel walls vibration. Neither the boundary condition (2.10) a) nor the boundary condition (2.10) b) correspond to reality, because both the inlet flow velocity and the inlet pressure should fluctuate as it was observed in the measurements [14]. Such a behaviour is nicely recovered using the penalization approach, see Figures 8 and 9.

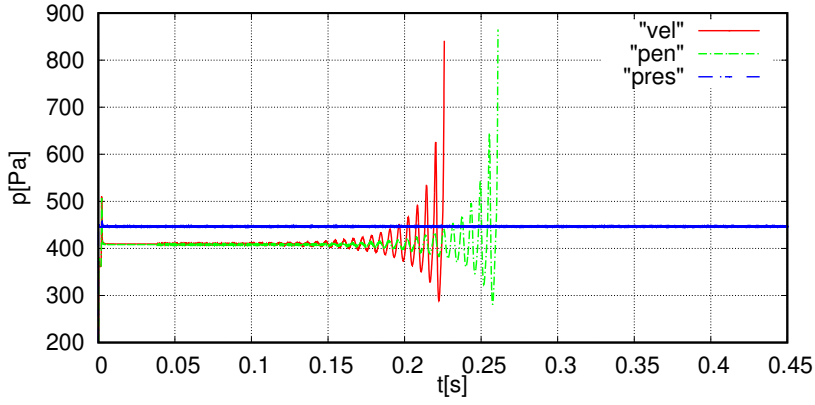

Figure 9. Pressure difference between inlet and outlet part of boundary in cases "vel", "pen" and "pres".

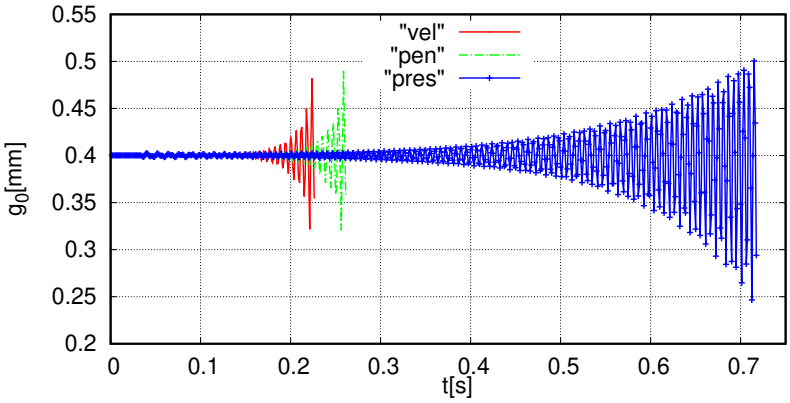

Figure 10. Time development of half-gap plotted for cases "vel", "pen" and "pres".

Figures 8–10 document that the penalization approach is a generalization of the Dirichlet boundary condition and the prescribed pressure drop boundary condition. They support the characteristic behaviour in the form of switching between these two types of boundary conditions in accordance to the chosen parameter ε.

Let us explain that in all three cases the considered inlet flow velocity exceeds the stability limit given by the critical flutter velocity, see [25]. Consequently, the magnitude of structural vibration amplitudes are exponentially increasing and the simulation in all three cases ends by the fluid flow solver failure. This is caused by a too distorted fluid computational mesh near the top of the elastic body although the considered half-gap is still large enough. This is partly due to the fact that here a more general motion of the structure is regarded.

4.2. The boundary of the flutter instability. Here, the self-induced vibrations of the vocal folds model were studied for prescribed penalization inflow boundary conditions (2.10) c) with penalization parameter $\varepsilon = 10^{-5}\,\mathrm{s/m}$. The displacement of the point S on the top of the vocal fold surface is plotted in Figure 11 for three different inlet flow velocities leading to three different types of behaviour of the FSI system.

For the inlet velocity $v_{\mathrm{dir},1} = 1.7\,\mathrm{m/s}$ (case C) the vibrations are damped and after a short transition regime the amplitudes decrease to a very low level of stationary vibrations. For the inlet velocity $v_{\mathrm{dir},1} = 1.77\,\mathrm{m/s}$ (case B) the displacements of the point S remained irregular but with limited maximal vibration amplitudes. This is quite typical response of FSI systems close to the aeroelastic stability boundary, see e.g. the so-called intermittent regimes in [31]. For the inlet velocity $v_{\mathrm{dir},1} = 1.79\,\mathrm{m/s}$ (case A) the magnitude of the vibrations is exponentially growing. We note that the vibration amplitudes in y-direction were of about one order less than in x-direction

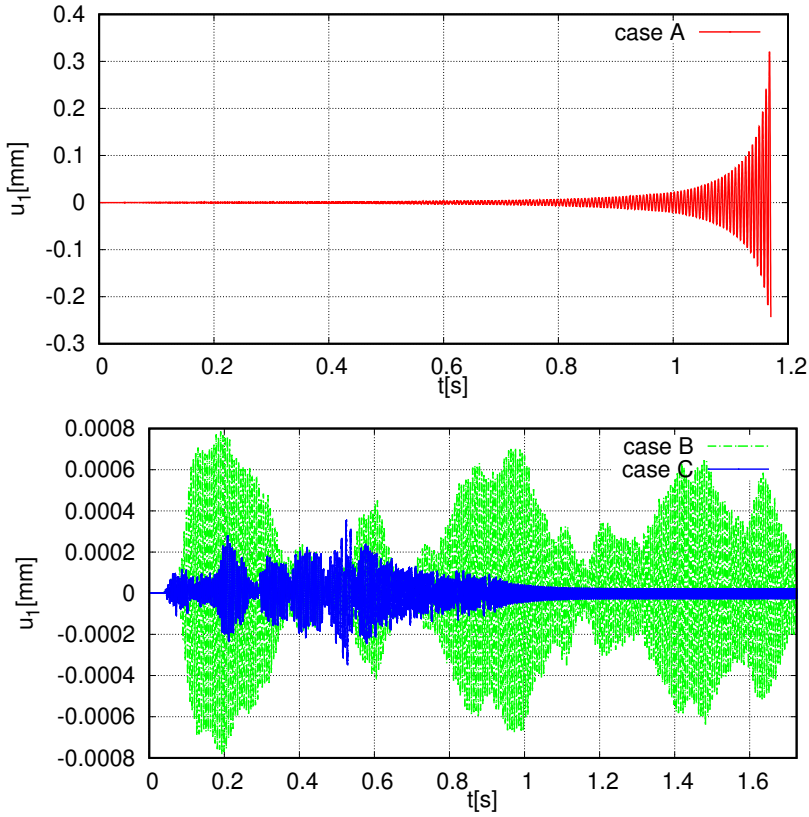

Figure 11. The time development of u_1 (x-component of displacement) for point S is shown in the case of three different inlet velocities: A) 1.79 m/s, B) 1.77 m/s, and C) 1.7 m/s, all prescribed by penalization approach. Note the different scaling of axes for the top and the bottom figure.

but with the same behaviour in the time domain as shown in Figure 11. Therefore, the critical flutter velocity is determined as $v_{\text{flutter}} \approx 1.78\,\text{m/s}$ for this model setting, which corresponds approximately to the results in [25], where $v_{\text{flutter}} \approx 1.85\,\text{m/s}$ was obtained for the simplified 2DOF vocal fold model.

Further, in the case of inlet velocity $v_{\text{dir},1} = 1.79\,\text{m/s}$ (case A) above the critical flutter velocity the unstable vibrations can be also illustrated by the energy of elastic body E^{s} approximated as

$$E^{\text{s}} = E^{\text{s}}_{\text{kin}} + E^{\text{s}}_{\text{pot}} = \frac{1}{2}\int_{\Omega^{\text{s}}} \varrho^{\text{s}}\dot{\mathbf{u}}^2\,\mathrm{d}x + \frac{1}{2}\int_{\Omega^{\text{s}}} (\lambda^{\text{s}}\,\mathrm{div}\,\mathbf{u}\delta_{ij} + 2\mu^{\text{s}}e^{\text{s}}_{ij}(\mathbf{u}))e^{\text{s}}_{ij}(\mathbf{u})\,\mathrm{d}x \approx \frac{1}{2}\dot{\mathbf{u}}^T\mathbb{M}\dot{\mathbf{u}} + \frac{1}{2}\mathbf{u}^T\mathbb{K}\mathbf{u}, \tag{4.3}$$

see Figure 12. The total energy E^{s} of the vibrating vocal folds model increases rapidly in the time domain.

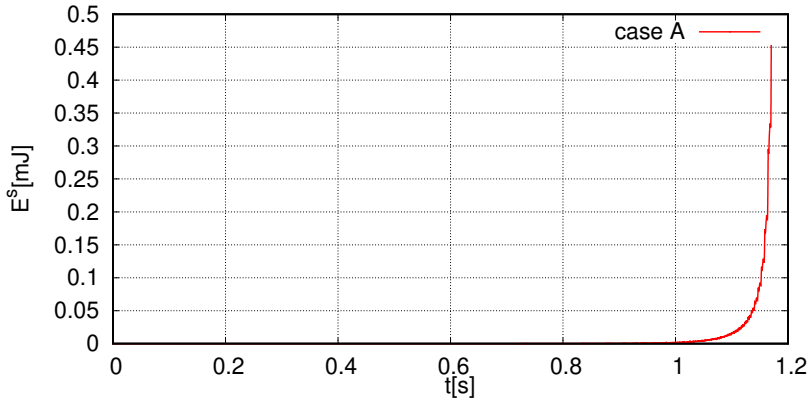

Figure 12. The time evolution of total energy of the elastic body Ω^{s} for flutter instability given by the inlet flow velocity 1.79 m/s (case A).

The flutter vibration has dominant frequency at about 169 Hz as seen from the Fourier transform of x- and y-displacement of the point S in Figure 13. The dominant frequency corresponds to a frequency between the second and the third eigenfrequency of the elastic body, see Figure 14.

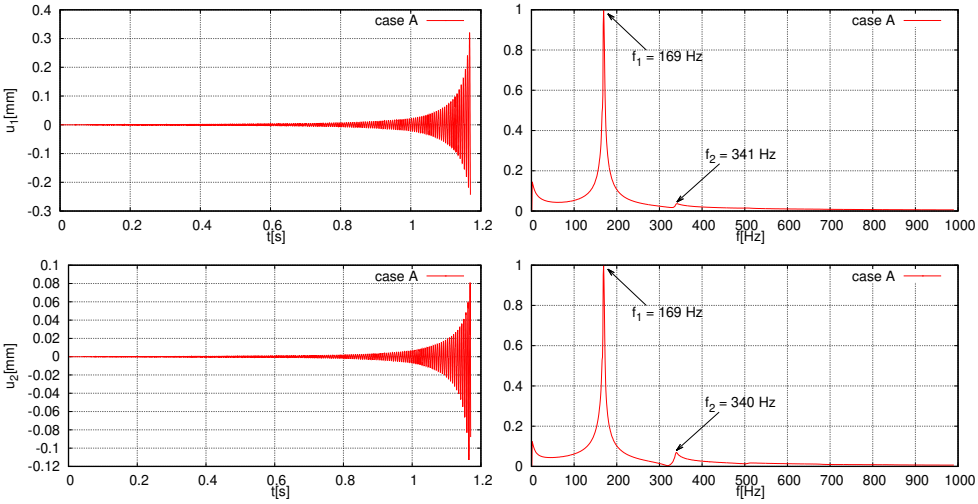

Figure 13. On the top—left: the displacement in x direction of point S, right: its the (normalized) Fourier transform. On the bottom—left: the displacement in y direction of point S, right: its the (normalized) Fourier transform. The all graphs are related to the prescribed inlet velocity $v_{\mathrm{dir},1} = 1.79\,\mathrm{m/s}$ (case A).

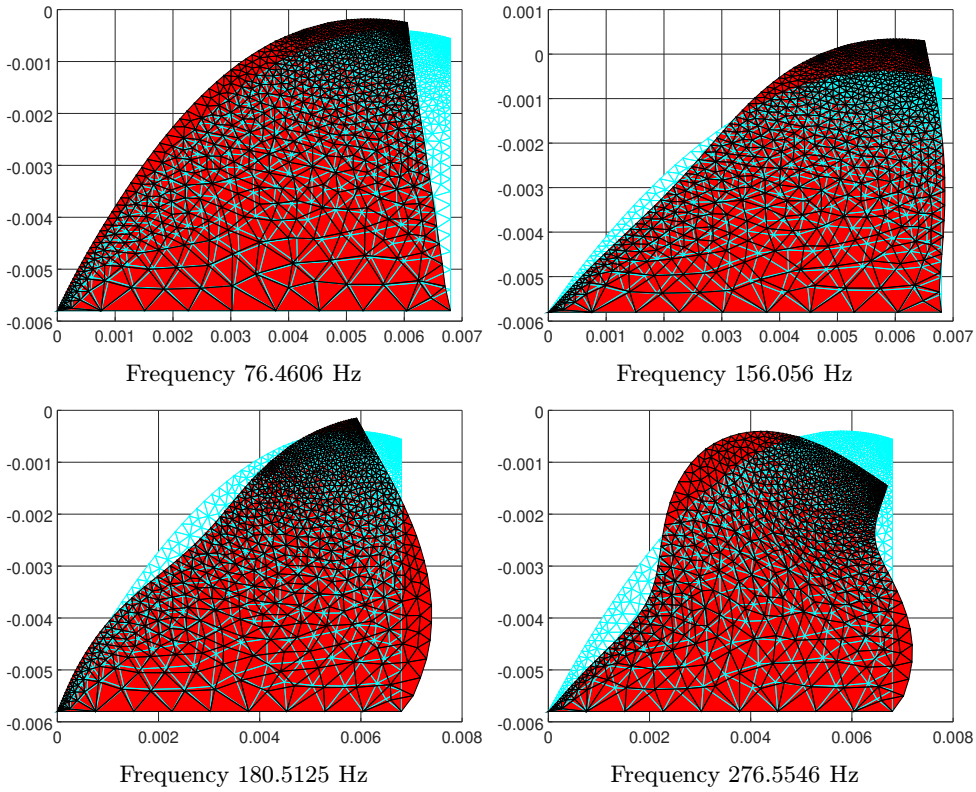

Figure 14. Modal analysis of the vibrating structure showing eigenmode shapes of vibration for first four eigenfrequencies 76.5 Hz, 156.1 Hz, 180.5 Hz and 276.6 Hz.

5. Conclusion

The mathematical problem of the fluid-structure interaction was described with special attention paid to the inlet boundary conditions. The penalization approach was introduced in detail as a generalization of the Dirichlet and the do-nothing boundary condition. The fluid flow was described by Navier-Stokes equations in the ALE form, where for modelling of the elastic body the linear elasticity was used.

The elasticity as well as fluid flow problem was numerically solved by the finite element method. The derivation of weak formulation was performed in details for different boundary conditions. Especially the SUPG, PSPG and 'div-div' stabilization was used for the flow solver. The ALE mapping was constructed with an aid of pseudo-elastic approach, where along the symmetry boundary the tangential displacement was kept free.

The numerical results achieved with the in-house developed program showed that the penalization approach is promising for FSI simulations of flow in cases of a periodical closing of the channel. This approach allows to relax the exact value of the inlet velocity on the boundary together with controlling the upper bound of the pressure drop between the inlet and outlet during channel closing phase. The performed parametric study gives approximate relations helping with the choice of a suitable magnitude of the penalization parameter for different FSI configurations. Finally, the flutter velocity for given settings was determined in a good correspondence to the reference results, i.e., the penalization approach did not change the aeroelastic stability boundary of the system. Next investigation could consist in introducing the time variation of the penalization parameter ε in relation to the time variation of the channel closing.

References

[1] *I. Babuška*: The finite element method with penalty. Math. Comput. *27* (1973), 221–228. zbl MR doi

[2] *T. Bodnár, G. P. Galdi, Š. Nečasová,* (eds.): Fluid-Structure Interaction and Biomedical Applications. Advances in Mathematical Fluid Mechanics, Birkhäuser/Springer, Basel, 2014. zbl MR doi

[3] *M. Braack, P. B. Mucha*: Directional do-nothing condition for the Navier-Stokes equations. J. Comput. Math. *32* (2014), 507–521. zbl MR doi

[4] *A. Curnier*: Computational Methods in Solid Mechanics. Solid Mechanics and Its Applications 29, Kluwer Academic Publishers Group, Dordrecht, 1994. zbl MR doi

[5] *D. J. Daily, S. L. Thomson*: Acoustically-coupled flow-induced vibration of a computational vocal fold model. Comput. Struct. *116* (2013), 50–58. doi

[6] *T. A. Davis*: Direct Methods for Sparse Linear Systems. Fundamentals of Algorithms 2, Society for Industrial and Applied Mathematics (SIAM), Philadelphia, 2006. zbl MR doi

[7] *N. G. Diez, S. Belfroid, J. Golliard,* (eds.): Flow-Induced Vibration & Noise. Proceedings of 11th International Conference on Flow Induced Vibration & Noise. TNO, Delft, The Hague, The Netherlands, 2016.

[8] *E. H. Dowell*: A Modern Course in Aeroelasticity. Solid Mechanics and Its Applications 217, Springer, Cham, 2004. zbl MR doi

[9] *M. Feistauer, J. Hasnedlová-Prokopová, J. Horáček, A. Kosík, V. Kučera*: DGFEM for dynamical systems describing interaction of compressible fluid and structures. J. Comput. Appl. Math. *254* (2013), 17–30. zbl MR doi

[10] *M. Feistauer, P. Sváček, J. Horáček*: Numerical simulation of fluid-structure interaction problems with applications to flow in vocal folds. Fluid-Structure Interaction and Biomedical Applications (T. Bodnár et al., eds.). Advances in Mathematical Fluid Mechanics, Birkhäuser/Springer, Basel, 2014, pp. 321–393. zbl MR doi

[11] *L. Formaggia, N. Parolini, M. Pischedda, C. Riccobene*: Geometrical multi-scale modeling of liquid packaging system: an example of scientific cross-fertilization. 19th European Conference on Mathematics for Industry (2016), 6 pages. doi

[12] *T. Gelhard, G. Lube, M. A. Olshanskii, J.-H. Starcke*: Stabilized finite element schemes with LBB-stable elements for incompressible flows. J. Comput. Appl. Math. *177* (2005), 243–267. zbl MR doi

[13] *V. Girault, P.-A. Raviart*: Finite Element Methods for Navier-Stokes Equations. Theory and Algorithms. Springer Series in Computational Mathematics 5, Springer, Cham, 1986. zbl MR doi
[14] *J. Horáček, V. V. Radolf, V. Bula, J. Košina*: Experimental modelling of phonation using artificial models of human vocal folds and vocal tracts. Engineering Mechanics 2017 (V. Fuis, ed.). Brno University of Technology, Faculty of Mechanical Engineering, 2017, pp. 382–385.
[15] *J. Horáček, P. Šidlof, J. G. Švec*: Numerical simulation of self-oscillations of human vocal folds with Hertz model of impact forces. J. Fluids Struct. *20* (2005), 853–869. doi
[16] *J. Horáček, J. G. Švec*: Aeroelastic model of vocal-fold-shaped vibrating element for studying the phonation threshold. J. Fluids Struct. *16* (2002), 931–955. doi
[17] *J. Horáček, J. G. Švec*: Instability boundaries of a vocal fold modelled as a flexibly supported rigid body vibrating in a channel conveying fluid. ASME 2002 International Mechanical Engineering Congress and Exposition. American Society of Mechanical Engineers, 2002, pp. 1043–1054. doi
[18] *C. Johnson*: Numerical Solution of Partial Differential Equations by the Finite Element Method. Cambridge University Press, Cambridge, 1987. zbl MR
[19] *M. Kaltenbacher, S. Zörner, A. Hüppe*: On the importance of strong fluid-solid coupling with application to human phonation. Prog. Comput. Fluid Dyn. *14* (2014), 2–13. zbl doi
[20] *G. Link, M. Kaltenbacher, M. Breuer, M. Döllinger*: A 2D finite-element scheme for fluid-solid-acoustic interactions and its application to human phonation. Comput. Methods Appl. Mech. Eng. *198* (2009), 3321–3334. zbl MR doi
[21] *H. Sadeghi, S. Kniesburges, M. Kaltenbacher, A. Schützenberger, M. Döllinger*: Computational models of laryngeal aerodynamics: Potentials and numerical costs. Journal of Voice (2018). doi
[22] *J. H. Seo, R. Mittal*: A high-order immersed boundary method for acoustic wave scattering and low-Mach number flow-induced sound in complex geometries. J. Comput. Phys. *230* (2011), 1000–1019. zbl MR doi
[23] *P. Šidlof, J. Kolář, P. Peukert*: Flow-induced vibration of a long flexible sheet in tangential flow. Topical Problems of Fluid Mechanics 2018 (D. Šimurda, T. Bodnár, eds.). Institute of Thermomechanics, The Czech Academy of Sciences, Praha, 2018, pp. 251–256. doi
[24] *W. S. Slaughter*: The Linearized Theory of Elasticity. Birkhäuser, Boston, 2002. zbl MR doi
[25] *P. Sváček, J. Horáček*: Numerical simulation of glottal flow in interaction with self oscillating vocal folds: comparison of finite element approximation with a simplified model. Commun. Comput. Phys. *12* (2012), 789–806. doi
[26] *P. Sváček, J. Horáček*: Finite element approximation of flow induced vibrations of human vocal folds model: effects of inflow boundary conditions and the length of subglottal and supraglottal channel on phonation onset. Appl. Math. Comput. *319* (2018), 178–194. MR doi
[27] *N. Takashi, T. J. R. Hughes*: An arbitrary Lagrangian-Eulerian finite element method for interaction of fluid and a rigid body. Comput. Methods Appl. Mech. Eng. *95* (1992), 115–138. zbl doi
[28] *J. Valášek, M. Kaltenbacher, P. Sváček*: On the application of acoustic analogies in the numerical simulation of human phonation process. Flow, Turbul. Combust. (2018), 1–15. doi
[29] *J. Valášek, P. Sváček, J. Horáček*: Numerical solution of fluid-structure interaction represented by human vocal folds in airflow. EPJ Web of Conferences *114* (2016), Article No. 02130, 6 pages. doi
[30] *J. Valášek, P. Sváček, J. Horáček*: On finite element approximation of flow induced vibration of elastic structure. Programs and Algorithms of Numerical Mathematics 18. Proceedings of the 18th Seminar (PANM), 2016. Institute of Mathematics, Czech Academy of Sciences, Praha, 2017, pp. 144–153. zbl MR doi

[31] *J. Venkatramani, V. Nair, R. I. Sujith, S. Gupta, S. Sarkar*: Multi-fractality in aeroelastic response as a precursor to flutter. J. Sound Vib. *386* (2017), 390–406. doi
[32] *S. Zorner*: Numerical Simulation Method for a Precise Calculation of the Human Phonation Under Realistic Conditions. Ph.D. Thesis, Technische Uuniversität Wien, 2013.

Authors' addresses: *Jan Valášek* (corresponding author), *Petr Sváček*, Department of Technical Mathematics, Faculty of Mechanical Engineering, Czech Technical University in Prague, Karlovo nám. 13, Praha 2, Czech Republic and Center of Advanced Aerospace Technology, Faculty of Mechanical Engineering, Czech Technical University in Prague, Technická 4, 166 07, Praha 6, Czech Republic, e-mail: `jan.valasek1@fs.cvut.cz`, `petr.svacek@fs.cvut.cz`; *Jaromír Horáček*, Institute of Thermomechanics of the Czech Academy of Sciences, Dolejškova 1402/5, 182 00 Praha 8, Czech Republic, e-mail: `jaromirh@it.cas.cz`.